DESIGN ANALYSIS AND EXPERIMENTAL VALIDATION OF RELAXATION OSCILLATOR-BASED CIRCUIT FOR R-C SENSORS

MOHAMAD IDRIS WANI¹, SADAN SAQUIB KHAN¹, BENISH JAN¹, MERAJ AHMAD², MARYAM SHOJAEI BAGHINI³, LAXMEESHA SOMAPPA³, AND SHAHID MALIK¹

ABSTRACT. Relaxation oscillator-based circuits are widely used for interfacing various resistive and capacitive sensors. The electrical equivalent of most resistive and capacitive sensors is represented using a parallel combination of resistor and capacitor. The relaxation oscillator-based circuits are not suitable for parallel R-C sensors. In this paper, we propose a modified circuit for parallel R-C sensors. The proposed relaxation oscillator-based circuit is based on a dual-slope and charge transfer technique to measure the resistance and capacitance of parallel R-C sensors separately. In addition, the paper provides a detailed analysis and design considerations for the oscillator design by taking into account the various sources of non-idealities. A method to reduce the error by using single-cycle averaging is also introduced. To verify the analyzed design criteria, the circuit is tested with multiple operational amplifiers with different non-idealities. Experimental results verify the performance of the proposed circuit. The circuit is tested for a range from 10 pF to 42 pF and 100 k Ω to 1 M Ω for parallel R-C sensors with an error of less than 1.5%. The circuit is tested with a fabricated water-level sensor. The result confirms the efficacy of the proposed circuit.

Introduction

Resistive and capacitive sensors are very popular and widely used in the scientific, biomedical, and industrial applications for measurement of force, displacement, pressure, humidity, temperature, liquid level, and bio-medical implants [1, 2, 3, 4, 5]. The signal conditioning circuits for these sensors are generally based on bridge-based circuits, relaxation oscillator-based resistance/capacitance to frequency converters, and direct digital converters [6, 7, 8, 9]. Bridge circuits are the fundamental building block for resistance measurement. Wheatstone bridge-based circuits are preferred for measuring a small variation in sensor resistance. However, the single-element resistive sensors' output voltage is non-linear with respect to the change in the sensor resistance [10]. This is especially critical when the sensor resistance change is large compared to the baseline resistance. This affects the sensitivity for wide dynamic range measurement. On the other hand, the relaxation oscillator-based circuits provide a wide-dynamic range measurement of sensor resistance by linearly converting the resistance into frequency.

Most of the signal conditioning circuits for resistive and capacitive sensors are based on the assumption that the sensor is ideal and can be represented by either a resistor in the case of the resistive sensors or a capacitor in the case of the capacitive sensors [6, 9, 11, 12, 13]. However, the assumption is not valid for many sensing applications. For instance, the resistive sensors are affected by a parasitic capacitance [2]. Similarly, most of the capacitive sensors are affected by a leakage resistance [14, 15]. Therefore, the electrical equivalent circuit for most of the resistive and capacitive sensors consists of a resistor and capacitor in parallel [2]. In such sensors, one component carries information about the measurand, while the other component is present because of the non-ideal nature of the sensor which is unpredictable. Therefore, its

1

effect should be compensated at the circuit level, or it degrades the performance of the sensor system. Moreover, in some sensors, both sensing components are a function of the measurand and need simultaneous measurement [16, 17].

The signal conditioning circuits for the parallel R-C sensors are mostly based on the phase-sensitive detection (PSD) technique. The PSD-based techniques require an in-phase and a quadrature reference signal to separately measure the resistance and capacitance of the parallel R-C sensors. Auto-nulling and PSD-based signal conditioning circuits for the parallel R-C sensors are reported in [18, 19, 20]. These circuits periodically provide the measurement of the R-C parameters of the sensor. However, it requires analog multipliers and an auto-nulling loop, which increases the complexity and power consumption. Another PSD-based signal conditioning circuit for parallel R-C sensors is reported in [21]. The circuit provides simultaneous measurement of sensor capacitance and resistance. However, the output of the signal conditioning circuit is sensitive to many circuit parameters and component non-idealities, which affects the robustness of the sensor system. Moreover, the output voltage is sensitive to noise, affecting the measurement's resolution.

Thanks to the inherent properties such as the quasi-digital output and high noise immunity, the relaxation oscillator-based circuits are preferred for lossless resistive, and capacitive sensors [7, 8, 22, 23] as shown in Fig. 1. The oscillator-based circuit reported in [23, 24, 25] are designed for the measurement of larger variation in sensor resistance with parasitic capacitance. However, the design considerations for the desired accuracy are not presented in [23, 24]. Another oscillator-based signal conditioning circuit for parallel R-C sensors is reported in [14]; however, the measurement range for the capacitance measurement is very small (<1 pF). This limits the range of applications of the circuit reported in [14].

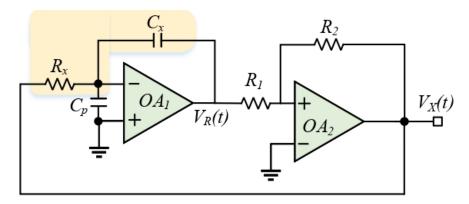


FIGURE 1. Schematic diagram of the relaxation oscillator circuit for resistive/capacitive sensor. In the case of an ideal capacitive sensor, C_x is the sensing variable, and R_x is the integrator resistance. In the case of an ideal resistive sensor, R_x is the sensing element, and C_x is the integrator capacitance as a reference element.

The initial results of the relaxation-oscillator circuit for capacitance measurement are reported in [25]. In this paper, we present the extended analysis, design considerations, experimental validation of the performance parameters, and sensor testing with the relaxation oscillator-based signal conditioning circuits. The features of the paper are highlighted as follows.

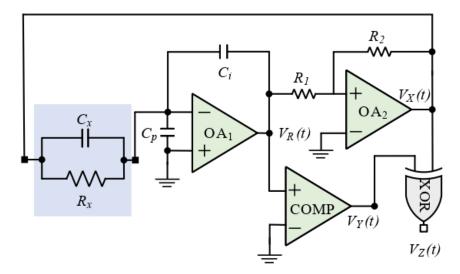


FIGURE 2. Schematic diagram of the proposed modified relaxation oscillator for parallel R-C sensors

- The proposed oscillator combines dual-slope and charge-transfer techniques to separately measure the resistance and capacitance of the parallel R-C sensors.
- Detailed analysis, including various sources of non-idealities, is included in the paper. The effect of various component non-idealities on the measurement of sensor parameters is analyzed.
- A single-cycle averaging method is utilized, which significantly reduces the effects of component non-idealities on the measurement of sensor parameters.
- The design criteria for the selection of components for designing the proposed signal conditioning circuit are also included in the paper.
- The proposed circuit is tested for different sensing conditions and the measurement is compared with the derived analytical solution.

Conventional Relaxation Oscillator for Resistive-Capacitive Sensors

The schematic diagram of the relaxation oscillator-based signal conditioning circuit (with triangular and square wave output) for resistive and capacitive sensors is shown in Fig. 1. The circuit consists of an integrator and a Schmitt trigger. The operational amplifier OA_1 along with the resistance R_x and capacitor C_x form the integrator of the oscillator. In the case of a capacitive sensor, C_x is replaced by the sensor element, and R_x is implemented using a known resistor. Similarly, in the case of resistive sensors, R_x is the sensor element (considered to be lossless in Fig.1), and C_x is the reference element. The signal conditioning circuits based on the conventional relaxation oscillator for resistive and capacitive sensors are reported in [7, 8, 22].

The integrator output in Fig. 1 is compared with the threshold voltage of the Schmitt trigger (implemented using R_1 , R_2 , and Op-Amp OA_2). The expression for the voltage $V_R(t)$ can then be derived as follows.

$$(1) V_R(t) = -\frac{1}{R_x C_x} \int_0^t V_p dt$$

where V_p is the peak voltage at the output of the Schmitt trigger. The threshold voltage of the Schmitt trigger is given as $\pm V_p \times (R_1/R_2)$. The capacitor C_x is initially charged with voltage $|V_p|$ at t=0. At t=T/2, the voltage $V_R(t)$ can be written as follows.

(2)
$$V_R\left(t = \frac{T}{2}\right) = -\frac{T V_p}{2 R_r C_r} = -2 V_p \frac{R_1}{R_2}$$

The expression of the oscillation time-period T of the square-wave output signal $V_X(t)$ can be derived as follows.

(3)
$$T = 4 R_x C_x \frac{R_1}{R_2}$$

The expression (3) indicates that the period T of the square-wave output of the relaxation oscillator circuit is proportional to the sensor variables (either C_x or R_x at once). However, the conventional relaxation oscillator circuit in Fig. 1 is not suitable for the leaky capacitive and parallel R-C sensors.

The accuracy of the relaxation oscillator based circuits for sensing applications are highly dependent on the symmetrical output in both positive and negative polarity. This can either be achieved using a network of Zener diodes or by using a rail-to-rail operational amplifier for the Schmitt trigger. Further, a current limiting resistor can also be used to ensure the safety [26]. In this paper, we are assuming the output voltage of the Schmitt trigger is symmetrical.

Modified Relaxation Oscillator for Impedance R-C Sensors

The modified relaxation oscillator circuit with the parallel R_x and C_x (electrical equivalent of a resistive sensor) at the inverting terminal of the integrator is shown in Fig. 2. The capacitor C_x is active only during the switching of square-wave voltage $V_X(t)$ from low to high and vice-versa. Charge transfer occurs between the capacitors C_x and C_i , during each of these transitions. For the rest of the cycle, the capacitor C_i charges/discharges through R_x with a linear slope. C_p is the parasitic capacitance of op-amp.

Oscillator Operating Principle The expression for the voltage $V_R(t)$ in Fig. 2 can be derived as follows.

(4)
$$V_R(t) = \left(\frac{R_1}{R_2} - \frac{2C_x}{C_i}\right) V_p - \int_0^t \frac{V_p}{R_x C_i} dt$$

The factor $2C_x/C_i$ is due to the charge transfer between C_x and C_i . The sudden charge transfer during the transition affects the initial voltage at the output $V_R(t)$. At t = T/2, $V_R(t)$ can be simplified as follows.

(5)
$$V_R(t) = \left(\frac{R_1}{R_2} - \frac{2C_x}{C_i}\right)V_p - \frac{TV_p}{2R_xC_i} = -V_p\frac{R_1}{R_2}$$

Therefore, the oscillation period, T at the output node V_x can be expressed as follows.

(6)
$$T = 4 R_x C_i \left(\frac{R_1}{R_2} - \frac{C_x}{C_i} \right)$$

The oscillation period T at the output node V_x of the circuit in Fig. 2 is proportional to R_x and C_x . However, the expression of time-period T is not enough to separately estimate both the capacitance C_x and resistance R_x of the sensor. Hence, additional information is necessary to measure both parameters separately.

To measure both the parameters R_x and C_x , a zero-crossing-detector (ZCD) (implemented using OA_3) and an XOR gate is added to separate the sensor components $(R_x \& C_x)$ into an

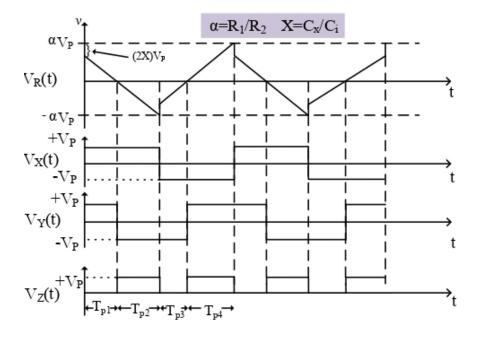


FIGURE 3. Timing diagram of the proposed oscillator shown in Fig. 2

equivalent pulse width. The ZCD separates the ramp signal into two parts: The first part is proportional to the charge transfer, and the second part is proportional to sensor resistance as represented by T_{p1} and T_{p2} in Fig. 3. The expression for T_{p1} and T_{p2} can be derived as follows.

(7)
$$T_{p1} = R_x C_i \left(\frac{R_1}{R_2} - \frac{2 C_x}{C_i} \right)$$

(8)
$$T_{p2} = R_x C_i \frac{R_1}{R_2}$$

The expression of unknown impedance (R_x, C_x) can be estimated as from T_{p1} and T_{p2} as follows.

(9)
$$C_x = \frac{R_1}{R_2} \frac{C_i}{2} (1 - \frac{T_{p1}}{T_{n2}})$$

(10)
$$R_x = \frac{R_1}{C_i R_2} T_{p2}$$

Oscillator Performance Analysis with Component Non-idealities

The developed relaxation oscillator circuit's output periods are affected by many circuit parameters and must be analyzed to design the circuit for a desired target resolution. The following non-idealities are considered.

- Op-Amp finite GBW, $A_0\omega_0$
- Op-Amp input bias current, ib

- Op-Amp slew rate, SR
- Schmitt trigger and Op-Amp offset voltage, Vos
- ZCD comparator offset, Voz
- ZCD comparator response delay, $\tau_{\rm Z,LH}$, $\tau_{\rm Z,HL}$
- Schmitt trigger response delay, $\tau_{S,LH}$, $\tau_{S,HL}$

The propagation time of the XOR gate will also affect the periods. The parasitic capacitance of the XOR gate also contributes to the propagation time. Usually, the propagation time of the XOR gate is in ns, which is smaller than the zero crossing detector and Schmitt trigger used in the circuit. Therefore, the effect of the XOR gate can be considered negligible for the circuit. Further, the effect of the propagation time of the XOR gate can be considered in the equation by adding the rise and fall time with the comparator output.

The steps for analyzing the effect of component nonidealities on the measurement of sensor parameters are as follows.

- (1) First, we will analyze the effect of the op-amp nonidealities on the slope and the offset of the integrator. The change in the integration slope and the effective integrator output offset is the primary concern for the oscillators' performance.
- (2) Next, we consider the effect of the oscillation period due to the component non-idealities in the ZCD and the Schmitt trigger with the non-ideal integrator output applied.
- (3) Finally, we will combine all the non-idealities to derive the oscillation period at the output of the XOR gate.

The detailed analysis of the component non-idealities is as follows.

Effect of the op-amp non-idealities on the slope and the offset of the integrator

First, considering finite GBW product, the integrator output voltage when driven by a unit step voltage V_p can be derived as follows.

(11)
$$V_R(s) = \frac{-V_p A_0 \omega_0}{s^2 R_x (C_x + C_p + C_i)} \left(\frac{1 + s C_x R_x}{s + \left(\frac{A_o \omega_0 R_x C_i + 1}{R_x (C_x + C_p + C_i)} \right)} \right)$$

The time domain voltage V_R(t) is obtained by transforming Eq. 11 into the time-domain

(12)
$$V_{R}(t) = V_{p}(\alpha - 2X) - \frac{V_{p}}{R_{x}C_{i}} \left\{ \underbrace{\frac{1}{\left(1 + \frac{1}{A_{0}\omega_{0}R_{x}C_{i}}\right)}}_{\text{Integration slope reduction due to finite GBW}} - \underbrace{\frac{1}{\left(1 + \frac{1}{A_{0}\omega_{0}R_{x}C_{i}}\right)^{2}} \frac{1}{A_{0}\omega_{0}} \left[1 + \left(\frac{C_{x} + C_{p}}{C_{i}}\right) + \frac{C_{x}}{C_{i}} \left(1 + A_{0}\omega_{0}R_{x}C_{i}\right)\right] e^{-\left(\frac{A_{o}\omega_{0}R_{x}C_{i}+1}{R_{x}(C_{x}+C_{p}+C_{i})}\right)t}}\right]}_{\text{Offset voltage due to finite GBW}}$$

and taking the initial value of $V_R(t)$ as $V_P(\alpha - 2X)$ where, $\alpha = R_2/R_1$ and $X = C_x/C_i$. The time-domain voltage expression at node V_R is derived in Eq. 12. The integrator output voltage contains additional terms due to the Op-Amp non-idealities as seen from Eq. 12.

- The first term indicates that the finite GBW product reduces the slope of the linear ramp voltage at the integrator output by a factor $1 + 1/(A_o \omega_0 R_x C_i)$.
- The second term offers insight into the offset voltage introduced at the integrator output due to the finite GBW product and additionally due to the impedance/leaky-capacitive

sensor. The effect of the exponential transient term is small enough to be neglected. We denote the final offset term introduced due to finite GBW by γ and is given by

(13)
$$\gamma = \left(1 + \frac{C_x + C_p}{C_i} + \frac{C_x}{C_i} (1 + A_0 \omega_0 R_x C_i)\right) \frac{A_0 \omega_0 R_x C_i}{(1 + A_0 \omega_0 R_x C_i)^2}$$

Further, considering the Op-Amp in the integrator has an offset voltage of V_{os} and a bias current of i_b , the total offset voltage presented by the integrator is then $V'_{os} = V_{os} + i_b R_x$. A similar analysis of the integrator with a finite GBW Op-Amp in the presence of this offset term shows that the effect is evaluated simply by shifting the input by the equivalent offset voltage. Further, the slope of the integrator output waveform (triangular) is limited by the slew rate (SR) of the Op-Amp used in the integrator. Hence, the slope (SL) of the integrator output is given by Eq. 14, where the positive sign corresponds to $SL_{(-)}$, and the minus sign corresponds to $SL_{(+)}$.

(14)
$$SL = min \left\{ \frac{V_p \pm (V'_{os} + i_b R_x)}{R_x C_i \left(1 + \frac{1}{A_0 \omega_0 R_x C_i}\right)}, SR \right\}$$

Referring to Fig. 3, we now obtain the individual expressions for T_{P1} and T_{P2} to obtain the R_x and C_x value, which is the measurement parameter. Referring to Fig. 3, T_{P1} can be expressed as,

(15)
$$T_{P1} = max \left\{ \left[\frac{(\alpha - \gamma - 2X - V_{oz}/V_p)}{1 + (V'_{os} + i_b R_x)/V_p} \right] R_x C_i \right.$$

$$\cdot \left. \left(1 + \frac{1}{A_0 \omega_0 R_x C_i} \right), \frac{(\alpha - 2X)V_p}{SR} \right\}$$

Similarly, T_{P2} can be obtained as,

(16)
$$T_{P2} = max \left\{ \left[\frac{(\alpha + \gamma + V_{oz}/V_p)}{1 + (V'_{os} + i_b R_x)/V_p} \right] R_x C_i \right.$$

$$\cdot \left(1 + \frac{1}{A_0 \omega_0 R_x C_i} \right), \frac{(\alpha - 2X)V_p}{SR} \right\}$$

Timing non-idealities in the ZCD and the Schmitt trigger Considering the rise and fall times of the Schmitt trigger and the ZCD as: $\tau_{S,HL}$ and $\tau_{S,LH}$ be the high to low and low to high response delays of the Schmitt trigger and $\tau_{Z,HL}$ and $\tau_{Z,LH}$ be high to low and low to high response delays of the ZCD, the expression of T_{P1} and T_{P2} in Eq. 15 and Eq. 16, are refined as Eq. 17 and Eq. 18, respectively.

Combined effect of the non-idealities on the measurement From the combined non-idealities represented in Eq. 18, the expression for the sensor resistance R_x can be inferred as

$$T_{P1} = max \left\{ R_x C_i(\alpha - 2X) \left[\frac{1 - \frac{\gamma + V_{oz}/V_p}{\alpha - 2X}}{(1 + V'_{os}/V_p)} \right] \left(1 + \frac{1}{A_0 \omega_0 R_x C_i} \right), \frac{(\alpha - 2X)V_p}{SR} \right\} + \frac{\tau_{S,LH} + \tau_{Z,LH}}{2}$$

(18)
$$T_{P2} = max \left\{ R_x C_i \alpha \left[\frac{1 + \frac{\gamma + V_{oz}/V_p}{\alpha}}{(1 + V'_{os}/V_p)} \right] \left(1 + \frac{1}{A_0 \omega_0 R_x C_i} \right), \frac{(\alpha - 2X)V_p}{SR} \right\} + \frac{\tau_{S,HL} + \tau_{Z,LH}}{2}$$

follows.

(19)
$$R_x = \frac{T_{P2}}{\alpha C_i} \left[\frac{1}{\beta_1} - \frac{\alpha}{A_0 \omega_0} \right]$$

where

(20)
$$\beta_1 = \frac{1 + (\gamma + V_{oz}/V_p)/\alpha}{1 + V'_{os}/V_p}$$

The expression for the R_x shows that the sensor parameter is significantly affected by the non-idealities of the circuit components. Similarly, for the capacitive sensors and parallel R-C sensors, the measurement capacitor C_x can be derived from Eq. 17 and Eq. 18 as follows.

(21)
$$C_{x} = \frac{\alpha C_{i}}{2 + \left(\frac{A_{0}\omega_{0}R_{x}C_{i}}{1 + A_{0}\omega_{0}R_{x}C_{i}}\right)} \left[1 - \left(\frac{T_{P1}}{T_{P2}}\right) \left(\frac{1 + V'_{os}/V_{p}}{\frac{1}{\beta_{1}} - \frac{\alpha}{A_{0}\omega_{0}}}\right) \left(\frac{1}{1 + \frac{1}{A_{0}\omega_{0}R_{x}C_{i}}}\right) - \frac{V_{oz}}{\alpha V_{p}}\right]$$

Eq. 19 and Eq. 21 provide the measured sensor capacitance and sensor resistance values R_x and C_x with the component non-idealities. The ideal values of measured sensor resistance and capacitance, are: $R_x = \frac{T_{P2}}{\alpha C_i}$ and, $C_x = \frac{\alpha C_i}{2} (1 - \frac{T_{P1}}{T_{P2}})$. Comparing the R_x and C_x values obtained from Eq. 19 and Eq. 21 with the ideal values, it is evident that there is a large error introduced due to the component non-idealities.

The analytical solution for C_x and R_x derived in Eq. 21 and Eq. 19 is evaluated by including the non-idealities of commercial operational amplifiers. The results show that even for a precision op-amp such as OPA177FP from Analog Devices, the worst-case error in the measurement due to component non-idealities is as high as 30% for R_x measurement and 60% for C_x measurement.

Accuracy Enhancement with Single Cycle Averaging

The timing waveform of the proposed circuit with an offset voltage V_{os} due to component non-idealities is shown in Fig. 4. The ideal timing waveform T_{p1} , T_{p2} , T_{p3} , and T_{p4} are shown in Fig. 4 as ideal $V_z(t)$. However, as derived in Eq. 12, the zero-crossing point of $V_R(t)$ is

(22)

$$T_{P3} = max \left\{ R_x C_i(\alpha - 2X) \left[\frac{1 + \frac{\gamma + V_{oz}/V_p}{\alpha - 2X}}{(1 - V'_{os}/V_p)} \right] \left(1 + \frac{1}{A_0 \omega_0 R_x C_i} \right), \frac{(\alpha - 2X)V_p}{SR} \right\} + \frac{\tau_{S,HL} + \tau_{Z,HL}}{2}$$

(23)
$$T_{P4} = max \left\{ R_x C_i \alpha \left[\frac{1 - \frac{\gamma + V_{oz}/V_p}{\alpha}}{(1 - V'_{os}/V_p)} \right] \left(1 + \frac{1}{A_0 \omega_0 R_x C_i} \right), \frac{(\alpha - 2X)V_p}{SR} \right\} + \frac{\tau_{Z,HL} + \tau_{S,LH}}{2}$$

shifted by an offset voltage V_{os} due to component non-idealities such as fine GBW and offset voltage of operational amplifiers. This affects the practical $V_z(t)$ as shown in Fig. 4. Consider T_{of} as the corresponding offset time between the ideal and the practical output waveform $V_z(t)$ due to finite offset voltage V_{os} . From Fig. 4, if T_{p1} switches from $-V_p$ to $+V_p$ by T_{of} time earlier than ideal, then T_{p3} will switch from $+V_p$ to $-V_p$ after T_{of} time compared to the ideal transition.

Therefore, the practical expression for time periods can be written as $T'_{p1} = T_{p1} - T_{of}$ and $T'_{p3} = T_{p3} + T_{of}$. The averaging of T'_{p1} and T'_{p3} will eliminate the effect of the mismatch in the time period between T_{p1} and T_{p3} . Same is true for T_{p2} and T_{p4} . Therefore, intuitively, it is possible to reduce the effect of component non-idealities by single-cycle averaging. It can be seen from the waveform that the pattern repeats after T'_{p4} . Therefore, averaging more than one cycle does not further enhance the accuracy of the sensor parameter measurement due to component non-idealities.

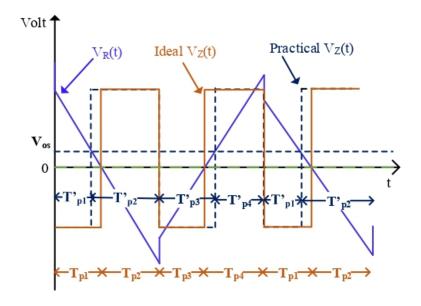


FIGURE 4. The ideal and practical $V_z(t)$ of the proposed relaxation oscillator based circuit shown in Fig. 2. The offset due to the component non-idealities is represented as V_{os} . This offset affects the period T_{p1} , T_{p2} , T_{p3} , and T_{p4} . The practical periods due the offset is represented by T'_{p1} , T'_{p2} , T'_{p3} , and T'_{p4} . Averaging the alternate cycles of practical $V_z(t)$ significantly reduces the error.

In order to analyze the effect of averaging, we have derived the expression for the period T_{p3} and T_{p4} in Eq. 22 and Eq. 23, respectively. The measurement of T_{p3} and T_{p4} is useful to understand the effect of non-idealities in the subsequent cycle of one complete cycle of $V_x(t)$.

(24)

$$T_{1} = \frac{T_{P1} + T_{P3}}{2} = max \left\{ R_{x}C_{i}(\alpha - 2X) \left[\frac{1 + \left(\frac{V'_{os}}{V_{p}}\right)\left(\frac{\gamma + V_{oz}/V_{p}}{\alpha - 2X}\right)}{1 - \left(V'_{os}/V_{p}\right)^{2}} \right] \left(1 + \frac{1}{A_{0}\omega_{0}R_{x}C_{i}} \right), \frac{2V_{p}(\alpha - X)}{SR} \right\} + \frac{\tau_{S} + \tau_{Z}}{2}$$

(25)

$$T_{2} = \frac{T_{P2} + T_{P4}}{2} = max \left\{ \alpha R_{x} C_{i} \left[\frac{1 - \left(\frac{V_{os}'}{\alpha V_{p}}\right) \left(\gamma + V_{oz}/V_{p}\right)}{1 - \left(V_{os}'/V_{p}\right)^{2}} \right] \left(1 + \frac{1}{A_{0}\omega_{0} R_{x} C_{i}} \right), \frac{2V_{p}(\alpha - X)}{SR} \right\} + \frac{\tau_{S} + \tau_{Z}}{2} \left(\frac{1 - \left(\frac{V_{os}'}{\alpha V_{p}}\right) \left(\gamma + V_{oz}/V_{p}\right)}{1 - \left(V_{os}'/V_{p}\right)^{2}} \right) \left(\frac{1 - \left(\frac{V_{os}'}{\alpha V_{p}}\right) \left(\gamma + V_{oz}/V_{p}\right)}{SR} \right) \right\}$$

The time periods T_{p1} and T_{p3} are averaged to obtain T_1 and, the time periods T_{p2} and T_{p4} are averaged to obtain T_2 . The expression of the averaged period T_1 and T_2 are derived in Eq. 24 and Eq. 25,(on page 11) respectively. The high-to-low and low-to-high response delays are assumed to be the same for the ZCD (τ_Z) and Schmitt trigger (τ_S) for deriving Eq. 24 and Eq. 25.

To observe and compare the enhancement in the accuracy due to averaging, consider the case when all the offsets are zero, the SR is not limited, and the only non-ideality is the limit on the GBW. For this case, the time expressions without and with averaging are derived in the subsequent subsections.

Without Averaging: T_{p1} and T_{p2} The Eq. 26 and Eq. 27 (on page 12) shows that the period T_{p1} and T_{p2} for the measurement of the sensor parameters are greatly affected by the gain-bandwidth products of the operational amplifiers. For instance, for OPA177, for an R_x of 330 k Ω and C_x of 33 pF, the error in the period T_{p1} and T_{p2} due to the GBW is 52.76% and 26.74%, respectively.

(26)
$$T_{P1} = R_x C_i (\alpha - 2X) \left(1 - \frac{\gamma}{\alpha - 2X} \right) \left(1 + \frac{1}{A_0 \omega_0 R_x C_i} \right)$$

(27)
$$T_{P2} = \alpha R_x C_i \left(1 + \frac{\gamma}{\alpha} \right) \left(1 + \frac{1}{A_0 \omega_0 R_x C_i} \right)$$

With Single Cycle Averaging: T_1 and T_2 Considering only the GBW of the operational amplifiers, T_1 and T_2 from Eq. 24 and Eq. 25 can be simplified as follows.

(28)
$$T_1 = R_x C_i(\alpha - 2X) \left(1 + \frac{1}{A_0 \omega_0 R_x C_i} \right)$$

(29)
$$T_2 = \alpha R_x C_i \left(1 + \frac{1}{A_0 \omega_0 R_x C_i} \right)$$

The offset, γ introduced due to the finite GBW of the Op-Amp severely affects the accuracy of time measurement as observed in Eq. 28 and Eq. 29 along with the slope reduction factor of $1 + 1/(A_o\omega_0R_xC_i)$. With averaging, the time accuracy is not dependant on the offset factor γ and depends only on the slope reduction factor as observed in Eq. 28 and Eq. 29. Therefore, the single-cycle averaging significantly reduces the error due to the GBW of the Op-Amps. For example, in the case of OPA177, with an R_x of 330 k Ω and C_x of 33 pF, the error in the period

 T_1 and T_2 due to the GBW is 1.5% and 0.72%, respectively, which is significantly smaller as compared to the measurement without averaging.

Design Criteria

The first design criterion is the selection of α , which decides the range of measurement. A higher value of C_x results in a higher factor X (i.e. C_x/C_i), which might result in a cross-over of the voltage beyond the zero value while charge transfer. To avoid this, we get the following condition on α

(30)
$$\alpha > 2 \frac{C_{x,max}}{C_i}$$

The error in capacitance measurement ϵ results in a worst-case error compared to the error in the resistance measurement. The error in capacitance measurement is the deviation of time T_1 from the ideal value.

(31)
$$\epsilon = \frac{\Delta C_x}{C_x} = \frac{\Delta T_1}{T_1}$$

 ΔC_x represents the incremental value of sensor capacitance and ΔT_1 represents the corresponding relative change measurement time.

Using Equations 24, 13 and, 31 the following conditions on the Op-Amp GBW, SR, offset can be arrived at,

(32)
$$\epsilon < \frac{100}{1 - \left(\frac{V'_{os}}{V_p}\right)^2} \left[\frac{1}{GBW(R_{x,min}C_i)} + \frac{V'_{os}}{V_p} \left(\frac{1}{\frac{\alpha C_i}{C_{x,max}} - 2} + \frac{V'_{os}}{V_p} \right) \right]$$

$$SR > \frac{2V_p}{R_{x,min}C_i}$$

For a given error tolerance in the measurement, an Op-Amp with a GBW and offset requirement and SR that satisfies Eq. 32 and Eq. 33 must be chosen. A comparator must also be selected with an offset value $V_{\rm oz} << V_{\rm p}$ and response time (τ) condition derived as follows.

(34)
$$\tau < \frac{\epsilon \alpha R_{x,max} C_i}{100 \left(1 - (V'_{os}/V_p)^2\right)}$$

Considering the propagation time of the XOR gate as τ_p , the XOR gate must be chosen based on the following equation.

(35)
$$\tau_p < \frac{\epsilon \alpha R_{x,max} C_i}{100 \left(1 - (V'_{os}/V_p)^2\right)} + \tau$$

Experimental Setup and Results

Several prototypes of the proposed relaxation oscillator-based signal conditioning circuit shown in Fig. 2 are built to illustrate the circuit's capabilities for measuring sensor capacitance and resistance. Different operational amplifiers are employed to implement the integrator, Schmitt trigger, and ZCD of the proposed oscillator and are tabulated in Table 1, further using these opamps, the effect of component non-idealities on the measurement of sensor parameters has been studied. All the passive components are first measured using a commercial table-top LCR meter (Agilent E4980A). The periods of the readout signal are measured using the timer/counter module of the microcontroller. In this experiment, we have used an Arduino

Op-Amp	$\mathrm{GBW}/(2\pi)$	SR	C_p	Vof	i_b	au
IC	(MHz)	$(V/\mu s)$	(\mathbf{pF})	(mV)	(nA)	(ns)
AD741	1	0.5	_	5	500	300
LT1360	60	800	4	0.3	250	_
TL071	5.25	29	2	4	0.1	310
OPA177	0.6	0.3	_	0.6	6	-
LT1049	0.8	0.8	_	0.01	0.05	_

Table 1. Operational amplifiers with performance parameters

Uno microcontroller with a 16-bit timer. The data from the microcontroller is acquired in MATLAB, and the single-cycle averaging is performed.

Multiple experiments were conducted to evaluate the performance of the proposed signal conditioning circuit. Initial experiments were conducted by emulating the sensor using discrete resistors and capacitors. The final experiment is conducted on a fringing field-based capacitive water level sensor. The sensor is emulated by placing known values of resistor R_x and capacitor C_x in parallel. The time period T_{p1} , T_{p2} , T_{p3} , and T_{p4} are measured to calculate the value of the sensor resistor.

Resistance Measurement

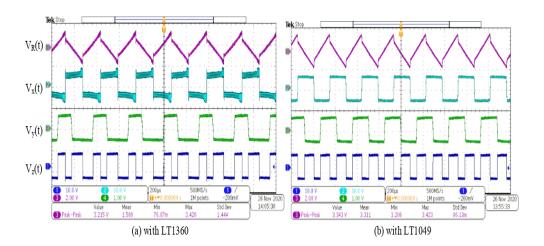


FIGURE 5. The waveform at different nodes of the oscillator developed using op-amp LT1360 and LTC1049. The voltage $V_R(t)$ is affected by the non-idealities of the op-amps, which affects the pulse width of $V_Y(t)$ (ideally should be 50% duty cycle). Due to this, the output $V_z(t)$ has different positive and negative pulse widths resulting in an error in the measurement of sensor parameters. (a) The error in the measurement is significant for LT1360, (b) the error is reduced with LTC1049 compared to LT1360. The error is negligible after a single-cycle averaging operation.

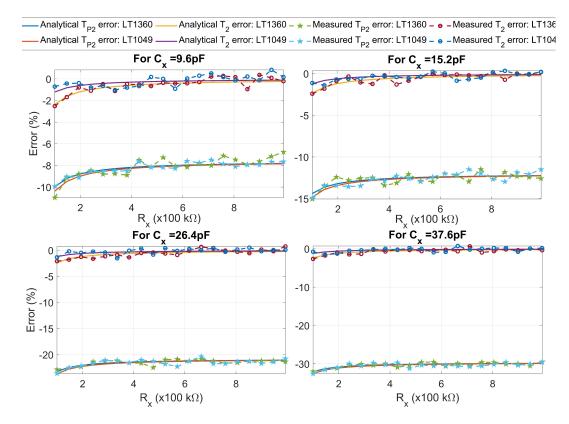


FIGURE 6. Measured and Analytical error in time $(T_2\&T_{P2})$ for different sensor capacitance C_x and resistance R_x for two the LT1360 and LTC1049. The analytical T_{p2} error is calculated from Eq. 18, which shows the error in the measurement due to component non-idealities. The analytical T_2 error shows the effect of single cycle averaging and is calculated from Eq. 25. The analytical and experimental error reduces significantly with single-cycle averaging.

The resistance (R_x) measurement is performed by measuring the period T_{p2} and T_2 (average of T_{p2} and T_{p4}). In addition to the measurement of the sensor resistance, the experiment also demonstrates the effect of component non-idealities on the measurement. The experiment is conducted as follows.

- (1) A capacitor C_x is placed in parallel with the sensor resistance R_x . The value of R_x is varied from 100 k Ω to 1000 k Ω . The period T_{p2} and T_{p4} is measured, and the percentage relative error is calculated with and without averaging.
- (2) The same process is repeated for multiple values of the capacitance C_x .
- (3) The above process is repeated for different operational amplifiers, and the effect of component non-idealities are evaluated on the measurement.

The percentage relative error for different values of the sensor resistance at different C_x values for the operational amplifiers LT1360 and LTC1049 are shown in Fig. 6. The result shows that the single cycle averaging significantly reduces the error in the measurement of the sensor resistance. The worst-case percentage relative error with and without single cycle averaging

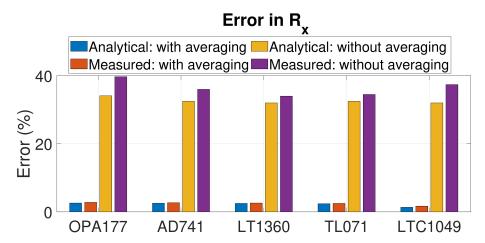


FIGURE 7. Analytical and measured worst-case error in sensor resistance R_x with different Op-Amps. The analytical error without averaging is calculated from Eq. 18. The analytical error with averaging is shown the effect of single cycle averaging and calculated from Eq. 25.

Table 2. Performance Parameters of the Developed Circuit

Parameters	Expression	Measurement				
1 arameters	Expression	C_x	R_x			
$\mathbf{SD}(\sigma)$	$\sqrt{\sum_{n=1}^{M} \frac{(S(n) - \overline{S})^2}{M - 1}}$	10.2fF	8.1 Ω			
SNR	$10 \log \frac{\sum_{n=1}^{M} (S(n))^2}{\sum_{n=1}^{M} (S(n) - \overline{S})^2}$	74.83 db	$78.96~\mathrm{db}$			
Dynamic Range	-	10pF-42pF	$100 \mathrm{k}\Omega$ - $1 \mathrm{M}\Omega$			
Worst		1.6 %	0.62%			
Relative Error	-					
$S(n)$ is the n^{th} measured value \bar{S} is the average value of the measurements						

for R_x measurement, for different operational amplifiers is shown in Fig. 7. The chart in Fig. 7 shows the choice of the operational amplifier and the effect of non-idealities. The % relative error is high for the operational amplifier OPA177, which has a low gain-bandwidth. Moreover, the % relative error is also high for LT1360, which has a good gain-bandwidth but has high input offset voltage. On the other hand, the error is small for LTC1049, which has a moderate gain-bandwidth and small input offset voltage. Therefore, the oscillator should be designed considering all the non-idealities of the operational amplifiers. The operational amplifiers' selection should be done based on the Eq. (33) and Eq. (35) from the design criteria for the given error.

Capacitance Measurement

In case of capacitance measurement, the value of sensor capacitor C_x is varied and the periods T_{p1} , T_{p2} , T_{p3} , and T_{p4} are measured experimentally. The experiment is conducted for different values of R_x . The experimental procedure for C_x measurement of impedance R-C or leaky capacitive sensors is as follows.

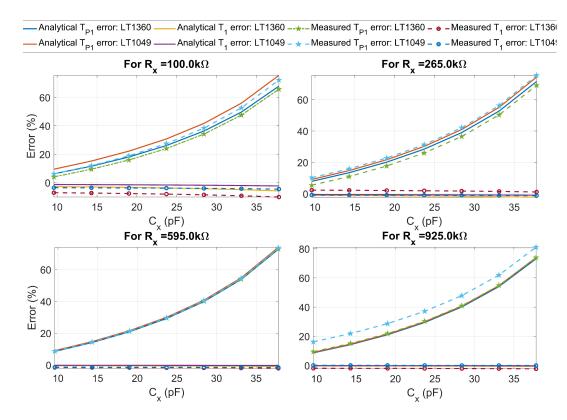


FIGURE 8. Measured and Analytical error for different sensor capacitance C_x and resistance R_x for two different Op-Amps.Analytical and measured worst-case error in sensor capacitance C_x with different Op-Amps. The analytical T_{p1} and T_1 errors are calculated from Eq. 15 and Eq. 24, respectively. The analytical T_{p1} shows the error due to component non-idealities. The analytical T_2 error shows the effect of single cycle averaging. The results are experimentally verified.

- (1) First, R_x is fixed at one value and C_x is varied from 9.6 pF to 37.6 pF.
- (2) Next, the same process is repeated for different R_x values. The experiment is conducted using different operational amplifiers.
- (3) The experimental results for different values of sensor capacitor C_x for operational amplifiers LT1360 and LTC 1049 are shown in Fig. 8.

The error is calculated from the measured time periods with and without single cycle averaging. The worst-case errors for different operational amplifiers are shown in Fig. 9. The single-cycle averaging dramatically reduces the percentage relative error for the measurement of sensor capacitance. The experimental results showing the pattern of error for different value of R_x by varying C_x from 10 pF to 42 pF is shown in Fig. 8. The experimental results shown in Fig. 8 are obtained for Op-Amps LT1360 and LTC1049. Results show that the percentage relative error is high for the LT1360, which is also justified analytically. On the contrary, the error is small for LTC1049. The experimental result follows the analytical model of the circuit.

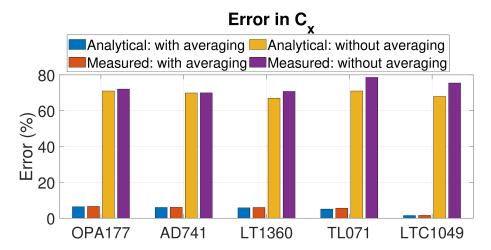


FIGURE 9. Analytical and measured worst-case error in sensor capacitance C_x with different Op-Amps. The analytical T_{p1} and T_1 errors are calculated from Eq. 15 and 24, respectively. The analytical T_{p1} shows the error due to component non-idealities. The analytical T_2 error shows the effect of single cycle averaging. The results are experimentally verified.

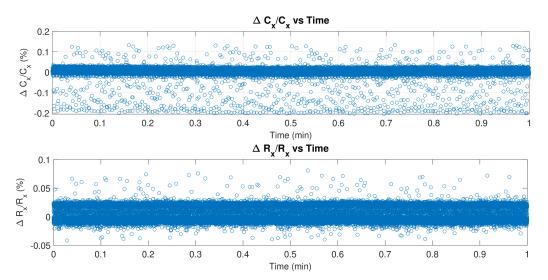


FIGURE 10. Measured $\Delta C_x/C_x$ and $\Delta R_x/R_x$ with time, for $C_x{=}$ 33 pF and $R_x{=}$ 330 k Ω

The single-cycle averaging reduces the error to a great extent.

Other Performance Parameters

Other performance parameters such as the standard deviation and SNR of the proposed relaxation oscillator circuit for R-C sensors is measured experimentally. The time period T_{p1} , T_{p2} , T_{p3} , and T_{p4} are experimentally recorded for a R_x and C_x values of 33 pF and 330 k Ω . The measured periods are averaged for C_x and R_x measurement and the $\Delta C/C_x$ and $\Delta R/R_x$ is

plotted in Fig. 10. The standard deviation and the SNR are calculated from the obtained data set using the expression mentioned in Table 2. The obtained standard deviation and SNR for C_x and R_x are reported in Table 2.

The circuit is tested for a capacitance as low as ten pF. At the lower capacitance value, the input capacitance of the operational amplifier is comparable with the sensor capacitance. Therefore, the relative error will be high at the lower capacitance value. However, the measurement can be performed by calibrating the effect of the input capacitance of the operational amplifier.

Testing with Water-Level Sensor The developed converter is utilized for the measurement of the sensor capacitor for the leaky capacitive water-level sensor. The water-level sensor is fabricated on a flexible substrate using the screen-printing technique. The sensor geometry is based on the inter-digitized electrodes. The principle of sensing is based on a change in the fringing field around the electrodes due to the water level, which in turn changes the capacitance of the sensor. The details of the sensor fabrication are reported in [27, 28].

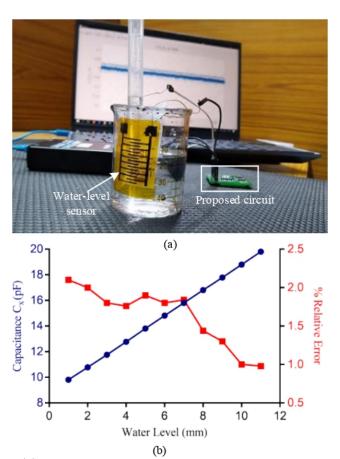


FIGURE 11. (a) Experimental setup for water-level leaky capacitive sensor, (b) experimental response of variation in the capacitance measured using the proposed circuit with multiple water levels. The sensor shows a 99.9% linear response with respect to the water-level.

TABLE 3. Performance Comparison of the Proposed Circuit with Other Reported Work

Output		Measurement Range		% Relative Error		SNR(db)		Technique	Power
		C_x pF	$R_x k\Omega$	C_x	R_x	C_x	R_x	rechnique	Consumption
This Work (LTC1049)	Pulse Width	10-42	100-1000	1.6	0.62	74.83	78.96	Oscillator	8.4 mW
[29]	Bit-Stream	100-200	700-900	±0.2	±0.2	-	-	Dual Slope	175 mW
[30]	Bit-Stream	50-1000	50-1000	0.73	0.82	64.35	70.87	Swithced-Capacitor	NA
[15]	Bit-Stream	150-206	>5000	1	-	-	-	Charge/Discharge	NA
[20]	Analog Voltage	100-2000	33-3000	6	8	-	-	PSD	168 mW
[18]	Analog Voltage	10-760	56-6500	± 0.11	± 0.07	49	50	Auto-Nulling	142 mW
[19]	Analog Voltage	200-100k	33-1200	10	100	-	-	Auto-Nulling	NA

The experimental setup for the system is shown in Fig. 11(a). The sensor is placed inside the beaker with known water levels. A controlled amount of water is poured into the beaker. The capacitance of the sensor is measured with the commercial LCR meter (Agilent E4980A) as well as with the proposed circuit. The percentage relative error in the measurement of the sensor capacitance for different water levels is shown in Fig. 11(b).

The experimental test was conducted with the oscillator circuit built using the LTC1049 operational amplifier. In addition, the R^2 value is estimated from the fitted experimental data and found to be 99.9%. This shows that the sensor shows a linear response to the water level. Further, the error reported in Table 2 is with the standard ceramic capacitors, while the error from the plot shown in Figure 11 is with the sensor. The mismatch in the error value is primarily because of the parasitic capacitance of the sensor-circuit interconnection and the measurement error.

Conclusion

A modified relaxation oscillator based signal conditioning circuit for parallel R-C sensors is presented in this paper. The proposed circuit is based on a dual-slope and charge-transfer technique embedded into a modified relaxation oscillator. Detailed analysis and design criteria of the proposed circuit design are provided, considering various sources of errors. A single-cycle averaging method is analytically derived, which significantly reduces the effect of component non-idealities. The efficacy of the proposed circuit is tested on the fabricated prototype. The measurement result shows the effectiveness of the proposed circuit for parallel R-C sensors. The performance parameters of the developed prototype are calculated. The proposed circuit provides an SNR of around 75 dB and 79 dB for capacitive and resistive sensors, respectively. Overall, the proposed circuit is well suited for various sensors such as leaky capacitive sensors, resistive sensors with a parasitic capacitor, and impedance R-C sensors.

References

- [1] L. Baxter, Capacitive Sensors Design and Application. New Delhi, India: Wiley-IEEE Press, 1997.
- [2] A. D. Marcellis and G. Ferri, Analog Circuit and System for Voltage-mode and Current-mode Sensor Interfacing Application, New Delhi, India: Springer, 2011.
- [3] S. Malik, M. Ahmad, M. Punjiya, A. Sadeqi, M. S. Baghini, and S. Sonkusale, "Respiration monitoring using a flexible paper based capacitive sensor," in Proc. IEEE Sensors 2018. New Delhi, India: IEEE, 2018.
- [4] F. Reverter, X. Li, and G. C. M. Meijer, "A novel interface circuit for grounded capacitive sensors with feedforward-based active shielding," Measurement Science and Technology, vol. 19, no. 2, p. 025202, jan 2008. [Online]. Available: https://dx.doi.org/10.1088/0957-0233/19/2/025202
- [5] A. Heidary and G. C. M. Meijer, "An integrated interface circuit with a capacitance-to-voltage converter as front-end for grounded capacitive sensors," Measurement Science and Technology, vol. 20, no. 1, p. 015202, nov 2008. [Online]. Available: https://dx.doi.org/10.1088/0957-0233/20/1/015202.

- [6] Ignjatovic and M. F. Bocko, "An interface circuit for measuring capacitance changes based upon capacitance-to-duty cycle (cdc) converter." IEEE Sensors J., vol. 5, no. 3, pp. 403–410, June 2005.
- [7] T. Islam, L. Kumar, Zaheeruddin, and A. Ganguly, "Relaxation oscillator-based active bridge circuit for linearly converting resistance to frequency of resistive sensor," IEEE Sensors J., vol. 13, no. 5, pp. 1507–1513, May 2013.
- [8] A. Cichocki and R. Unbehauen, "A switched-capacitor interface for capacitive sensors based on relaxation oscillators," IEEE Trans. Instrum. Meas., vol. 39, no. 5, pp. 797–799, Oct. 1990.
- [9] K. Kishore, S. Malik, M. S. Baghini, and S. A. Akbar, "A dual-differential subtractor-based auto-nulling signal conditioning circuit for wide-range resistive sensors," IEEE Sensors Journal, vol. 20, no. 6, pp. 3047–3056, 2020.
- [10] P. Ramanathan Nagarajan, B. George, and V. J. Kumar, "A linearizing digitizer for wheatstone bridge based signal conditioning of resistive sensors," IEEE Sensors Journal, vol. 17, no. 6, pp.1696–1705, 2017.
- [11] Ye, C. He, B. Liao, and J. Huang, "A new capacitance measuring system for capacitive sensor for moving target detection," IEEE Transactions on Circuits and Systems-II, vol. 12, no. 13, pp. 1–5, October 2018.
- [12] H. Hwang, H. Lee, M. Han, H. Kim, and Y. Chae, "A 1.8-v 6.9-mW 120-fps 50-channel capacitive touch readout with current conveyor AFE and current-driven ADC," IEEE Journal of Solid-State Circuits, vol. 53, no. 1, pp. 204–218, January 2018.
- [13] F. Reverter, X. Li, and G. C. M. Meijer, "Stability and accuracy of active shielding for grounded capacitive sensors," Measurement Science and Technology, vol. 17, no. 11, p. 2884, sep 2006. [Online]. Available: https://dx.doi.org/10.1088/0957-0233/17/11/004.
- [14] X. Li and G. C. M. Meijer, "An accurate interface for capacitive sensors," IEEE Trans. Instrum. Meas., vol. 51, no. 5, pp. 935–939, Oct. 2002.
- [15] F. Reverter and O. Casas, "A microcontroller-based interface circuit for lossy capacitive sensors," Meas. Sci. Technol., vol. 21, pp. 065 203–065 210, May 2010.
- [16] T. Shimamura et al., "Impedance-sensing circuit techniques for integration of a fraud detection function into a capacitive fingerprint sensor," IEEE Sensors J., vol. 12, no. 5, pp. 1393–1401, May 2012.
- [17] D. Zhang, J. Liu, and B. Xia, "Layer-by-layer self-assembly of zinc oxide/graphene oxide hybrid toward ultrasensitive humidity sensing," IEEE Electron Device Letters, vol. 37, no. 7, pp. 916–919, July 2016.
- [18] S. Malik, M. Ahmad, L. Somappa, T. Islam, and M. S. Baghini, "AN-Z2V: autonulling-based multimode signal conditioning circuit for R-C sensors," IEEE Transactions on Instrumentation and Measurement, vol. 69, no. 11, pp. 8763–8772, 2020.
- [19] P. Mantenuto, A. D. Marcellis, and G. Ferri, "Novel modified de-sauty autobalancing bridge-based analog interfaces for wide-range capacitive sensor applications," IEEE Sensors J., vol. 14, no. 5, pp. 1664–1672, May 2014.
- [20] S. Malik, K. Kishore, T. Islam, Z. Zargar, and S. Akbar, "A time domain bridge-based impedance measurement technique for wide-range lossy capacitive sensors," Sens. Actuators A, Phy., vol.234, pp. 248–262, Sept. 2015.
- [21] . U. Khan, T. Islam, B. George, and M. Rehman, "An efficient interface circuit for lossy capacitive sensors," IEEE Trans. Instrum. Meas., vol. 68, no. 3, pp. 829–836, March 2019.
- [22] Mochizuki, K. Watanabe, T. Masuda, and M. Katsura, "A relaxation-oscillator-based interface for high-accuracy ratiometric signal processing of differential-capacitance transducers," IEEE Trans. Instrum. Meas., vol. 47, no. 1, pp. 11–14, Feb. 1998.
- [23] A. D. Marcellis, A. Depari, G. Ferri, A. Flammini, D. Marioli, V. Stornelli, and A. Taroni, "A CMOS integrable oscillator-based front end for high-dynamic-range resistive sensors," IEEE Trans. Instrum. Meas., vol. 57, no. 8, pp. 1596–1604, Aug. 2008.
- [24] G. Ferri, V. Stornelli, A. D. Marcellis, A. Flammini, and A. Depari, "Novel cmos fully integrable interface for wide-range resistive sensor arrays with parasitic capacitance estimation," Sens. Actuators B, Chm., vol. 130, no. 1, pp. 207–215, March 2008.
- [25] S. Malik, M. Ahmad, L. Somappa, T. Islam, and M. S. Baghini, "Impedance-to-time converter circuit for leaky capacitive sensors with small offset capacitance," IEEE Sensors Letters, vol. 3, no. 7, pp. 1–4, July 2019.
- [26] S. Franco, Design with Operational Amplifiers and Analog Integrated Circuits, 3rd ed. USA: McGraw-Hill, Inc., 2001.
- [27] S. Malik, L. Somappa, M. Ahmad, S. Sonkusale, and M. S. Baghini, "A fringing field based screen-printed flexible capacitive moisture and water level sensor," in 2020 IEEE International Conference on Flexible and Printable Sensors and Systems (FLEPS), 2020, pp. 1–4.

- [28] R. N. Dean, A. K. Rane, M. E. Baginski, J. Richard, Z. Hartzog, and D. J. Elton, "A capacitive fringing field sensor design for moisture measurement based on printed circuit board technology," IEEE Transactions on Instrumentation and Measurement, vol. 61, no. 4, pp. 1105–1112, 2012.
- [29] P. Vooka and B. George, "A direct digital readout circuit for impedance sensors," IEEE Trans. Instrum. Meas., vol. 64, no. 4, pp. 902–912, April 2015.
- [30] V. Sreenath and B. George, "A switched-capacitor circuit-based digitizer for efficient interfacing of parallelR-C sensors," IEEE Sensors J., vol. 17, no. 7, pp. 2109–2119, April 2017.
- 1 Centre for Sensors, Instrumentation, and Cyber Physical System Engineering, Indian Institute of Technology, New Delhi, India
 - $^2\mathrm{James}$ Watt School of Engineering, University of Glasgow, United Kingdom
 - 3 Department of Electrical Engineering, Indian Institute of Technology Bombay, Mumbai, India $Email\ address$: smalik@iitd.ac.in